UC Irvine
UC Irvine Previously Published Works

Title

The Glacier and Land Ice Surface Topography Interferometer: An Airborne Proof-of-Concept Demonstration of High-Precision Ka-Band Single-Pass Elevation Mapping

Permalink

https://escholarship.org/uc/item/8758m601

Journal

IEEE Transactions on Geoscience and Remote Sensing, 49(2)

ISSN

0196-2892

Authors

Moller, Delwyn
Hensley, Scott
Sadowy, Gregory A
et al.

Publication Date

2011-02-01

DOI

10.1109/tgrs.2010.2057254

Copyright Information

Peer reviewed

The Glacier and Land Ice Surface Topography Interferometer: An Airborne Proof-of-Concept Demonstration of High-Precision Ka-Band Single-Pass Elevation Mapping

Delwyn Moller, Scott Hensley, Gregory A. Sadowy, Charles D. Fisher, Thierry Michel, Mark Zawadzki, *Member, IEEE*, and Eric Rignot

Abstract—As part of the NASA International Polar Year activities, a Ka-band cross-track interferometric synthetic aperture radar (SAR) recently demonstrated high-precision elevation swath mapping capability. This proof-of-concept instrument was achieved by interfacing two Ka-band slotted-waveguide antennas in a cross-track geometry and Ka-band electronics with the Jet Propulsion Laboratory's L-band uninhabited aerial vehicle SAR. Deployed on the NASA Gulfstream III, initial engineering flights in March and April 2009 marked the first airborne demonstration of single-pass cross-track interferometry at Ka-band. Results of a preliminary interferometric assessment indicate height precisions that, for a 3 m $\times$ 3 m posting, range from 30 cm in the near range to 3 m in the far range and greater than 5 km of swath over the urban areas imaged. The engineering flights were followed by a comprehensive campaign to Greenland in May 2009 for ice-surface topography mapping assessment. Toward that end, coordinated flights with the NASA Wallops Airborne Topographic Mapper lidar were conducted in addition to establishing ground calibration sites at both the Summit Station of the National Science Foundation and the Swiss Camp of the Cooperative Institute for Research in the Environmental Sciences. Comparisons of the radar-derived elevation measurements with both *in situ* and lidar data are planned for a subsequent paper; however, at this stage, a single data example over rugged ice cover produced a swath up to 7 km with the desired height precision as estimated from interferometric correlation data. While a systematic calibration, including assessment and modeling of biases, due to penetration of the electromagnetic waves into the snow cover has not yet been addressed, these initial results indicate that we will exceed our system requirements.

Index Terms—Ice, interferometry, radar.

I. INTRODUCTION AND MOTIVATION

THE estimation of the mass balance of ice sheets and glaciers on Earth is a problem of considerable scientific and societal importance. A key measurement to understanding, monitoring, and forecasting these changes is ice-surface topography, both for ice-sheet and glacial regions. Measurements over the major ice sheets have been achieved with satellite radar altimeters [1], airborne laser altimetry [2], and satellite laser altimetry [3]. Satellite radar altimetry is most accurate over flat areas but performs poorly over the steep coastal regions where most of the changes are localized. Airborne laser altimetry is more useful in these steep regions but is limited in spatial coverage and swath width (500 m), rendering it impractical for use at the continental scale over Antarctica. Satellite laser altimetry, while limited in swath coverage, has provided a time record over the lifetime of IceSAT, and the record is to be extended with the IceSAT II mission expected for launch in 2015. In the interim, airborne activities underway will provide some measurement continuity between IceSAT and IceSAT II.

The various altimeter observations have shown that changes in the polar regions are rapid (occurring over years instead of centuries or millennia) and significant (e.g., meter-scale lowering of ice surfaces instead of millimeters), with the coastal regions having more than half of the signal from the ice sheets. However, it is in the topographically rugged and temporally dynamic coastal regions where the spatial coverage limitations of a profiling sensor are most profound.

To adequately assess the dynamics and volume changes in glacial/coastal margins of the ice sheets, one requires a mapping capability that fills the gaps between altimeter tracks at sufficient resolution. Toward that end, Moller *et al.* [4] introduced the Glacier and Land Ice Surface Topography Interferometer (GLISTIN) concept: a Ka-band (system center frequency selected at 35.66 GHz, with 8.4-mm wavelength) single-pass cross-track radar interferometer that could provide satellite-based swath elevation maps and imagery between nadir tracks. GLISTIN would be capable of providing significant swath widths, cover the poles submonthly, and provide inherently variable spatial resolution: high spatial resolution for meter-scale vertical precision on glaciers and coastal regions and coarse spatial resolution for decimeter accuracy on ice-sheet interiors.

TABLE I
GLISTIN REQUIREMENTS FOR THE SPACEBORNE CONCEPT AND THE AIRBORNE PROOF-OF-CONCEPT DEMONSTRATION

		Requirement	
		Spaceborne	Airborne
Coverage		70km (Yields subseasonal complete coverage of Antarctica and Greenland)	>5km swath (10km goal) (IceSAT II track spacing can be 15 km in Greenland)
Glacier/Coastal	Accuracy	1m	0.5m
	Posting	100m x 100m	30m x 30m
Ice Sheet	Accuracy	10cm	10cm
	Posting	1km x 1km	100m x 100m

While measuring height changes on glaciers and ice sheets over time is integral to climate change research, there is also a considerable value in assembling precise and complete topography of ice-covered areas. Elevation data provide constraints on the driving stress of the ice, drainage basins, and roughness statistics, as well as surface features that can be tracked through time to detect ice motion and acceleration. This argues for a mapping sensor.

Before such a spaceborne campaign is feasible, it is imperative that an airborne proof-of-concept demonstration be conducted to provide a proof of concept of the proposed mapping methodology. In this paper, we describe an airborne implementation and first results from a measurement campaign that acquired Ka-band single-pass interferometric radar data over a significant swath. To our knowledge, these are the first measurements of their kind at millimeter-wave frequencies. Key features include the following.

1) The Ka-band center frequency maximizes the single-pass interferometric accuracy (which is proportional to the wavelength), reduces snow penetration (when compared with lower frequencies), and remains relatively impervious to atmospheric attenuation.
2) Imaging capabilities that are important for mapping large areas. Imaging allows features to be tracked with time for estimation of ice motion and reduces data noise when measuring topographic changes over rough surfaces of glaciers and coastal regions of ice sheets.

To achieve this demonstration in a timely and cost-effective manner, the NASA Jet Propulsion Laboratory's (JPL) L-band uninhabited aerial vehicle synthetic aperture radar (UAVSAR) [5] was adapted for Ka-band operation and successfully collected interferometric data in engineering checkout flights on March 13 and 16 and April 21 and 29, 2009, aboard the NASA Dryden Gulfstream III (G-III). This was followed by a comprehensive campaign to Greenland on May 1–13, 2009, where collaborative acquisitions with the NASA Wallops Airborne Topographic Mapper (ATM) laser altimeter [6] occurred coincident with in situ observations at the Swiss Camp of the Cooperative Institute for Research in the Environmental Sciences (CIRES) and calibration sites at both Swiss Camp and the Summit Station of the National Science Foundation (NSF).

The remainder of this paper is organized as follows. Section II discusses the requirements of the airborne sensor. Section III discusses the system implementation with focus on

the interferometric performance. Section IV details calibration and processing. Finally, Section V presents initial data and assesses the system performance from both the local engineering flights and Greenland.

II. REQUIREMENTS

Table I shows the science requirements for the spaceborne GLISTIN design and corresponding airborne requirements. From space, to obtain meaningful results on ice sheets based on existing observations and interpretation of the results, we estimate that surface elevation must be measured with a sub-10-cm accuracy on a 1-km scale in the interior and a few tens of centimeters at a spatial resolution of 100 m at the coast, where the kilometer-scale dimensions of glaciers demand finer resolution. Details of mission design and technology development in support of spaceborne feasibility can be found in [4], [7], and [8].

The corresponding airborne sensor performance requirements exceed that of the spaceborne sensor with the exception of swath coverage. A minimum swath of 5 km is required, noting that the intertrack spacing of IceSAT was approximately 15 km on the coastal regions of the ice sheets. Therefore, an airborne mapper could be used to provide valuable details between IceSAT and IceSAT II tracks, particularly in topographically dynamic regions such as the coastal zones.

Maximal scientific exploitation of the Ka-band interferometric elevation data involves detailed comparison with in situ ground truth and lidar elevation data that are currently the standard for measuring ice-sheet topography. These comparisons will be the topic of a subsequent paper; however, in this paper, we will provide estimates of the expected instrument accuracy and precision. Before proceeding with a precision and accuracy analysis, a brief discussion of the definition of elevation is given, and the conventions employed in this paper are defined.

Elevation can be defined in numerous ways to take into account the spatial extent of a pixel and ground cover. One way of defining the elevation is as a point measurement of the elevation of the "bare" surface height above some reference ellipsoid. This definition has the advantage of being sensor neutral and independent of pixel size (sometimes referred to as postspacing); however, it complicates the discussion of accuracy when a particular sensor is selected for measurement. First, either for radar or lidar measurements of elevation, the reported elevation is a power-weighted return of the reflected
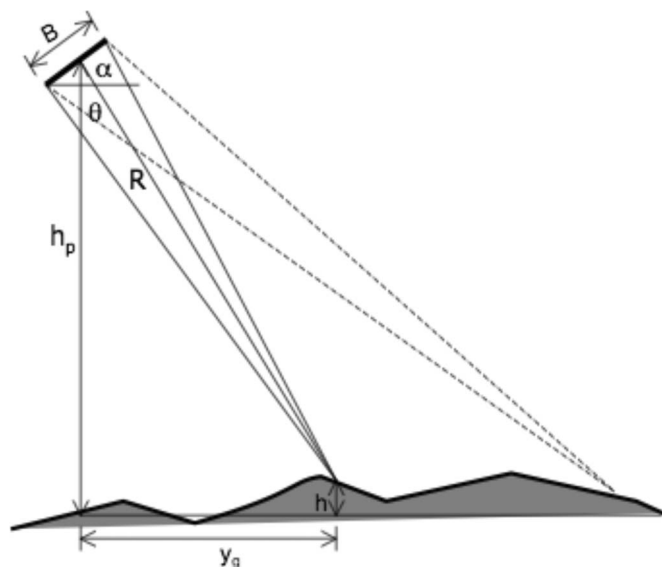
Fig. 1. Cross-track interferometer geometry for GLISTIN airborne implementation.

surface elevations within a resolution element of the sensor. Thus, there is an inherent "electromagnetic bias" term that must be evaluated that is a function of the resolution element size and the amount of elevation variation within the resolution element. Second, when the "bare surface" has some covering, either natural (e.g., vegetation, snow, etc.) or anthropogenic (e.g., building, power line, etc.), the electromagnetic bias is altered relative to a bare surface. The differing nature of the electromagnetic bias terms is particularly important when intersensor comparisons are being made. Since these analyses are being deferred to a subsequent paper, we adopt a radar interferometric sensor centric definition, similar to what was done for the Shuttle Radar Topography Mission, of elevation that simplifies our precision and accuracy analysis.

For the purposes of this paper, elevation is defined as the reflective surface elevation, i.e., backscatter-weighted average height over an output pixel area, relative to some reference ellipsoid, for example, WGS-84. The advantage of this definition is that we can avoid detailed discussions of the electromagnetic bias and directly relate the instrument precision to the interferometric correlation. The resulting accuracy will then follow from considerations of the sensor imaging geometry and onboard metrology systems (i.e., Inertial Navigation Unit (INU) and GPS) and the precision estimates.

A single-pass interferometric SAR (InSAR) is well suited to meet the stated requirements of Table I. When two antennas, displaced in the cross-track direction (as shown in Fig. 1), view the same region on the ground, the interferometric combination of data received on the two antennas allows one to resolve the path-length difference from the illuminated area to a fraction of a wavelength. From the interferometric phase, the height of the target (or phase center) can be estimated. Therefore, an InSAR system is capable of providing not only the position of each image point in along-track and slant range as with a traditional SAR but also the height of that point through the use of the interferometric phase [9], [10]. Deferring temporarily the evaluation of systematic errors until Section II, we can

express the elevation measurement error δh as a function of the baseline length B, the system frequency ($k = 2\pi/\lambda$), and the radar interferometric phase error $\delta\phi$

$$\delta h = -\frac{R\sin(\theta)}{kB\cos(\theta - \alpha)}\delta\phi \qquad (1)$$

where R is the range, θ is the look angle, and α is the baseline orientation angle, i.e., the angle that the baseline vector (vector between the two antenna phase centers) makes with respect to the local horizontal.

It is apparent, from the phase error term in (1), that high frequencies (with correspondingly larger wavenumbers k) maximize the interferometric accuracy for a given baseline length. This allows high-accuracy mapping from a system that fits in a compact volume suitable for airborne sensors. However, compact packaging was not the only consideration for selecting Ka-band for the ice mapping application. Since longer wavelength microwaves penetrate more deeply into the ice volume, we have selected as high a frequency as possible (with consideration to technology maturity and atmospheric attenuation) to minimize penetration, thus facilitating intercomparison with lidar sensor measurements. That said, it must be noted that knowledge of the penetration depth of Ka-band into snow is not well characterized or quantified due to lack of data. This provided a major motivation for this airborne validation.

To our knowledge, there are only a few experiments at Ka-band (0.8 cm) that examine the penetration depth[1] δ_p in ice. At 37 GHz, Ulaby *et al.* [11] quote δ_p of 20 cm for dry snow, lowering to 1 cm when the water content of snow increases from 0% to 4% in volume. (At C-band, the same model predicts > 10-m penetration depth in dry snow and 20 cm in 4% wet snow.) Penetration depth decreases when the snow grains are coarser. Ka-band signals strongly interact with snow grains (due to Mie scattering), whereas C-band ($\lambda \sim 5$ cm) signals are nearly transparent to dry snow. In general, models overestimate penetration depth in dry snow. Radar altimeters operating at Ku-band ($\lambda \sim 2$ cm) experience penetration depths in the range of several meters in Antarctica (from model inversion). Forsberg *et al.* [12] measured penetration depths up to 15 m in high altitudes with dry snow regions at Ku-band. Penetration within a medium depends on the dielectric losses (i.e., absorption and scattering) that strongly depend on wavelength. For small-scale scatterers, like snow grains, the scattering dependence on wavelength goes as a power of four [13]. Extinction being much higher at Ka-band, penetration reduces to less than 0.3 m as compared to several meters at Ku-band and is mainly due to scattering that increases by a factor of 55 [14]. Lytle and Jezek [15] measured permittivity of firn in Greenland over 26–40 GHz and estimated an upper limit loss of 5 dB/m, leading to a minimum penetration depth of 87 cm. These values for penetration depth represent an elevation bias that exceeds the surface elevation accuracy requirements (better then 10 cm) and do not consider variations with viewing geometry (e.g.,

[1]Note that penetration depth is the $1/e$ penetration depth or the depth at which the signal is attenuated to $1/e$ of its insertion value into the medium. This is not the interferometric height bias due to penetration into the medium which is of primary interest for mapping. However, the quantities are related as is discussed later.

incidence angle). Although penetration depth should be much smaller away from nadir, we expect penetration depths on the order of tens of centimeters in snow/ice at Ka-band with an InSAR instrument. Within the context of the requirements, this is a significant bias, and it is critical that we quantify the effective depth of penetration at the incidence angles of interest to validate this as an effective technique for airborne or spaceborne ice-surface topography mapping. As will be described in Section IV, collaborative flights with the NASA Wallops ATM occurred in Greenland in order to quantify the penetration and validate our models. Note that all the data collected over ground-truth sites (Swiss Camp and Summit) were under premelt extremely dry conditions. Our original intent of observing variation with snow wetness and melt was not achieved due to aircraft logistical constraints that arose during deployment. However, the comparative data and ground calibration survey targets will allow us to assess the limiting case where penetration is expected to be at a maximum, i.e., over the dry firn. This analysis is not complete and will be the subject of future publications.

III. System Design

A. System Implementation

In order to realize a cost-effective and timely demonstration of the GLISTIN concept, an adaptation to the NASA/JPL UAVSAR was proposed under the NASA International Polar Year program. UAVSAR is an airborne InSAR that is carried in an external pod on the NASA C-20 (G-III) aircraft [5]. UAVSAR is a complete turn-key SAR system that includes antenna, receivers, transmitter, timing and control, high-speed data recording, precision navigation and inertial measurement, and SAR ground data processing system. The UAVSAR is a facility instrument for NASA science investigations.

UAVSAR is operationally configured to support repeat-pass L-band (1.26-GHz) InSAR images with a bandwidth of 80 MHz. This is accomplished with a single electronically steered phased array antenna. Data from multiple passes over the same target area are used to form interferometric radar images. The radar pod that is mounted underneath the NASA G-III is equipped with its two differential GPS (DGPS) receivers and the Litton 251 blended INU/GPS that are used for motion metrology. DGPS data have a position accuracy of about 3–5 cm that has been verified using corner reflector data and repeat-pass radar interferometric data where we estimate the relative position error between repeat tracks. Estimated repeat-pass baselines are consistent with the 3–5-cm GPS position accuracy. In addition, factoring into the focusing performance is the attitude angle determination of the INU since the phase centers of the antennas are displaced from the INU motion reference point. Attitude measurement accuracy for the Litton 251 is about 10 arcseconds. The lever arm from the GPS antenna to the INU reference point was surveyed to millimeter accuracy, and the lever arm from the INU to the geometric center of the Ka-band antennas was also surveyed to a fraction of a millimeter in the aircraft body-fixed coordinate frame. Acceleration and velocity data (250- and 50-Hz sampling rates, respectively) are blended in a Kalman filter with DGPS data

(1 Hz) to provide high-accuracy Earth body-fixed position and velocity data (about 3–5 cm on all three axes) with relative position accuracy much better than 1/100 of a wavelength over the synthetic aperture length (about 300 m) needed for image focusing. The interferometric baseline was measured to about 0.1-mm accuracy. Image quality metrics, e.g., impulse response width and integrated sidelobe ratios, measured from corner reflectors indicate that our motion metrology system is performing as expected.

For our demonstration, we replaced the L-band phased array with a pair of Ka-band (35.66-GHz) slotted-waveguide antennas (detailed subsequently) that are configured as a single-pass cross-track interferometer. Both antennas were mounted to a single structure with the same mechanical interface as the UAVSAR L-band antenna.

Fig. 2 shows a block diagram of the Ka-band interferometer. Electronics that up- and downconvert between L- and Ka-bands and also a Ka-band traveling wave tube amplifier (TWTA) were borrowed from the Second-Generation Airborne Precipitation Radar (APR-2) [16] and integrated with UAVSAR to enable the Ka-band single-pass interferometric operation. As limited by the preexisting design, the transmitter did not switch between antennas (commonly referred to as "ping-pong") but used a single-transmit antenna, simultaneously receiving backscattered returns on both.

Table II gives the basic system parameters. The center frequency of 35.66 GHz falls within the Earth science frequency allocation band, and the 80-MHz bandwidth is compatible with the UAVSAR digital sampling hardware and results in ground-range resolutions varying from ∼6 m (incidence angle = 18°) in the near range to less than 3 m (incidence angle = 50°) in the far range. The transmit power of 35 W is the peak power at the antenna after accounting for waveguide losses from the TWTA in the cabin to the antenna in the pod.

The baseline geometry was chosen both for performance and to work within the UAVSAR pod and panel design. The antenna boresite of 31° off-nadir was found to minimize multipath scatter from the aircraft in electromagnetic simulations. However, the baseline angle of 45° was a constraint for compatibility with the UAVSAR pod geometry. For this reason, the antennas were canted with respect to the panel in which they mounted. The cross-track baseline was constrained to be less than 40 cm to fit within the panel. For performance reasons outlined subsequently, we chose $B = 25$ cm. Fig. 3 shows the reconfigured pod on the G-III with the two Ka-band antennas installed.

B. Antenna Design

The two antennas shown in Fig. 4 are identical, with uniformly distributed 2×80 waveguide slot arrays. The full 2×80 arrays are made up of two 2×40 half-arrays, each combined with an external two-way waveguide power divider. The 2×40 half-arrays are further subdivided into four 2×10 subarrays that are combined with an integrated power divider. Horizontal polarization was chosen to minimize mutual coupling. The antenna geometry is typical for slot arrays using a radiating layer with offset slots, a feed layer with angled coupling slots, and a power divider layer with offset input slots. In order
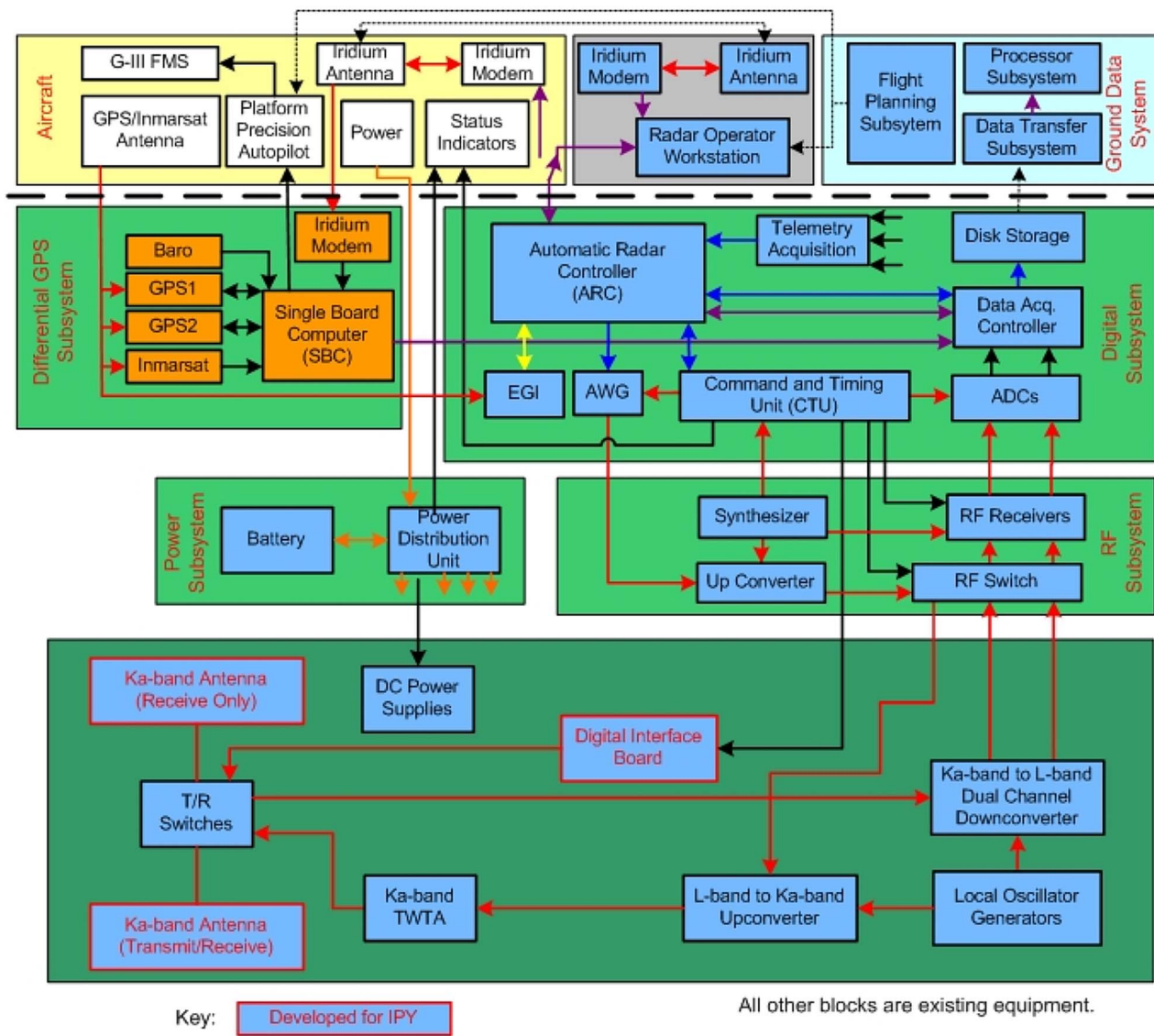
Fig. 2.   GLISTIN block diagram illustrating interface with UAVSAR and use of PR2 hardware for the IPY demonstration.

TABLE II
BASIC RADAR PARAMETERS

Parameter	Unit	Value
Center Frequency	GHz	35.66
Wavelength	mm	8.4
Peak Transmit Power (at antenna)	W	35.0
Antenna Width (physical – not radiating area)	cm	10
Antenna Length	cm	50
Polarization		Horizontal
3dB H-plane beamwidth	deg	35
3dB E-plane beamwidth	deg	0.9
Baseline	cm	25.0
Baseline Angle	deg	45.0
Bandwidth	MHz	80
Boresight Look Angle	deg	31.0
Duty Cycle	%	<10
Receiver Noise Figure	dB	6

Fig. 3.   Photograph of NASA G-III with pod configured for Ka-band interferometry. Lower inset shows a close-up with details of the two antennas.

to minimize development costs, the basic configuration—both mechanical and electrical—was kept as similar as possible to a prior design for GLISTIN technology development [8]. For
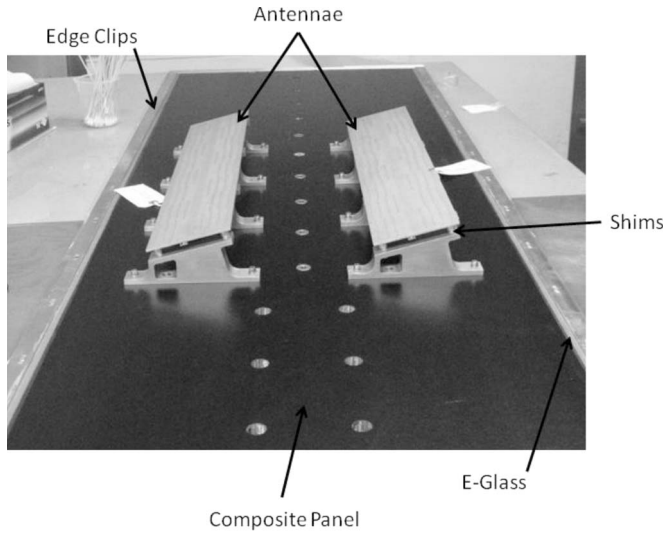
Fig. 4. Photograph of slotted-waveguide antennas mounted on low CTE composite panel. The panel measures 1748 mm long × 581 mm wide × 20.6 mm thick.

example, the relatively large waveguide power divider that combines the subarrays fits comfortably behind the aperture of the GLISTIN breadboard but consumes much of the footprint of the IPY array. This is the reason for the additional ground plane around the slots in the H-plane.

The antenna is directly exposed to the air stream, so a radome is required to protect it from the elements. The electrical performance of slot arrays is very sensitive to the proximate effects of dielectrics in terms of both return loss and pattern performance. A full-wave method-of-moments solution was not available to account for the radome, so commercial finite-element software (HFSS) was used to analyze the various radome options, including details such as adhesive layers with cutouts around the slots. The analysis assumed semi-infinite boundary conditions and included the angled coupling slot from the feed layer. The radome was originally intended to additionally protect the antenna from flying debris on takeoff and landings, but the options that used relatively thick dielectrics severely degraded the patterns. Since the antenna was located in an area that was unlikely to experience debris, a thin dielectric was selected as the best available option. Due to the uncertainties involved with knowledge of the dielectric constants and simulation errors—and because a second iteration of the antenna was not feasible—accommodations were made for a simple waveguide tuning iris at the input to the antennas. However, this step proved to be unnecessary based on voltage standing wave ratio measurements less than −10 dB.

C. Interferometric Design

A critical factor in the interferometric design is the baseline selection [9]. The height measurement sensitivity to the interferometric geometry shown in Fig. 1 is reflected in (1). The interferometric phase noise σ_ϕ as a function of interferometric correlation γ, a measure of similarity of the signals received by the two antennas in the interferometric pair, is given by

$$\sigma_\phi = \frac{1}{\sqrt{2N_L}} \frac{\sqrt{1-\gamma^2}}{\gamma} \qquad (2)$$

where N_L is the number of looks. The observed interferometric correlation for a single pass (i.e., simultaneous signal reception for the two antennas) can be conveniently expressed as the product of three terms, i.e., $\gamma = \gamma_n \gamma_g \gamma_v$, where γ_n is the correlation due to thermal noise given by

$$\gamma_n = \frac{1}{1 + SNR^{-1}}. \qquad (3)$$

with SNR being the signal-to-noise ratio. The geometric correlation γ_g is given by

$$\gamma_g = 1 - \frac{B\cos(\theta-\alpha)\Delta r}{\lambda R \tan(\theta)} \qquad (4)$$

where Δr is the radar slant-range resolution. The volumetric correlation γ_v, due to the vertical distribution of scatterers within a radar resolution element, is given by

$$\gamma_v = \frac{\int \sigma(z) e^{ik_z z}\, dz}{\int \sigma(z)\, dz} \qquad (5)$$

where k_z is the wavenumber in the vertical direction given by

$$k_z = \frac{B\cos(\theta-\alpha)}{\lambda R \sin(\theta)}. \qquad (6)$$

An estimate of the amount of volumetric correlation and interferometric penetration depth can be easily obtained if we assume a simple attenuating volume, i.e., $\sigma(z) = e^{-\eta z}$ (note that this model ignores Mie scattering effects and that more accurate model for comparison with Ka-band data will be the subject of a subsequent paper). Then, we have

$$|\gamma_v| = \frac{\eta\sqrt{\sinh^2\left(\frac{\eta d}{2}\right)\cos^2\left(\frac{k_z d}{2}\right) + \cosh^2\left(\frac{\eta d}{2}\right)\sin^2\left(\frac{k_z d}{2}\right)}}{\sqrt{\eta^2 + k_z^2}\,\sinh\left(\frac{\eta d}{2}\right)} \qquad (7)$$

where d is the depth of the volume. For the Ka-band mapper parameters at 35° incidence, we have $k_z = 0.09$ which gives a volumetric correlation of approximately 0.9999. The interferometric penetration depth (i.e., the elevation bias in the medium corresponding to the interferometric phase measurements) is estimated at 13 cm where we assumed that $d = 2\delta_p = 20$ cm, the electromagnetic penetration depth for 4% wet snow. Thus, the effective elevation bias for this simple model is somewhat larger than that desired for the ice mapping applications.

For an airborne single-pass system with sufficient ground resolution, the correlation is typically dominated by the system signal-to-thermal noise ratio (SNR). Thus, although greater accuracy is generally afforded by a larger baseline as shown in (1), it must be balanced against geometric correlation which, by (4), increases phase noise as the baseline increases. Volumetric correlation also decreases as the baseline increases depending on the amount of penetration, resulting in further phase noise increases.

An additional consideration further constraining the baseline is based on the phase-unwrapping process which occurs during interferometric processing of the data. As phase measurements are made only modulo 2π, but the phase resulting from the

TABLE III
PREDICTED INTERFEROMETRIC PERFORMANCE ACROSS THE SWATH FOR THE RADAR SYSTEM
CONFIGURATION ASSUMING "DRY SNOW" AND A 7-km ALTITUDE ABOVE GROUND

Common Parameters	Unit	Near (y=1.6km)	Mid (y=3.6km)	Far (y=6.6km)
One Look Azimuth Resolution	m	0.25	0.25	0.25
Ground Range Resolution	m	7.33	3.64	2.52
Geometric decorrelation		0.89	0.98	0.98
Noise Decorrelation		0.99	0.99	0.94
Interferometric Decorrelation		0.88	0.97	0.92
Ice Sheet Height Precision (100m x 100m Posting)				
Number of Looks in Azimuth	#	400	400	400
Number of Looks in Elevation (approx)	#	14	27	40
Total Number of Looks	#	5454	10987	15854
IF Phase Error	deg	0.30	0.10	0.14
Height Error	m	0.051	0.035	0.086
Glacier Height Precision (30m x 30m Posting)				
Number of Looks in Azimuth	#	120	120	120
Number of Looks in Elevation (approx)	#	4	8	12
Total Number of Looks	#	491	989	1427
IF Phase Error	deg	0.99	0.34	0.46
Height Error	m	0.08	0.06	0.14

differential range difference can be many multiples of 2π, it is necessary to adjust the measured phases by the correct multiple of 2π by enforcing continuity. Unwrapping becomes more difficult as the rate of phase change, which is a function of the baseline length and local slope, becomes large. Consequently, one must consider the relief of the scene when selecting the baseline. Over the glacial and coastal areas, relief can be significant (tens of degrees in slope $\Delta\tau$). The following can be used to constrain the baseline B:

$$B \leq \frac{\Delta\Phi_{\max}}{\Delta\tau_{\max}} \frac{R\sin(\theta)}{\Delta y_g k \cos(\theta - \alpha)} \qquad (8)$$

where Δy_g is the ground-range resolution.

By constraining the maximum interferometric phase variation across a pixel, $\Delta\Phi_{\max} = 30°$ for a slope of $\Delta\tau_{\max} = 30°$ resulted in a baseline of $B = 0.25$ m. This meets the maximum phase wrap-rate requirement down to an operating altitude of $H = 4$ km and gives $\Delta\Phi = 19°$ at a nominal altitude $h_p = 7$ km and cross-track slopes of $\Delta\tau = 30°$.

Table III shows the predicted performance at near, mid, and far swaths (corresponding to $\theta = 15°, 31°$, and $45°$, respectively) at an altitude of 7 km above ground. In these predictions, we assumed a normalized radar cross section σ_0 for dry snow [17] which is generally what we expect to encounter, particularly over the ice sheets. The predicted performance meets all the requirements over a 5-km swath in terms of *precision* (i.e., not accounting for penetration biases and other systematic error terms). Note that, for the glacier requirements, there is a significant performance margin and that well more than a 5-km swath may be achieved. However, in coastal regions, if the snow becomes wet, the σ_0 can drop by approximately 5 dB. Even so, for the glacial regions, a 6-km swath in terms of *precision* was predicted using the wet-snow profile.

To meet the accuracy requirements, either systematic error sources must be calibrated or the overall design must be such

that they are small enough to be neglected. The following are the dominant error sources:

1) relative phase drift of the receivers;
2) aircraft attitude knowledge uncertainty;
3) isolation between the receivers;
4) baseline change due to thermal distortions;
5) penetration into the snow cover which varies as a function of the snow wetnesss as described in (7).

Of these, items 1 and 2 can be modeled as an effective roll and manifest themselves as a tilt across the height map that, if slowly varying, can be corrected by calibration (discussed momentarily). For item 3, we measured the isolation in the Ka-band chain to exceed 70 dB, making this a negligible factor. For item 4, we levied a baseline stability requirement of $\delta B < 50\ \mu$m over a temperature range of $-70\ °C$ to $+70\ °C$ so that this error source could be effectively neglected. The design and implementation of the composite panel design that maintained the baseline are the topic of the next section. Finally, for item number 5, the modeling of the penetration is a topic of research, which, through collaborative acquisition and intercomparison with the ATM lidar sensor, will validate or calibrate model predictions. By removing or constraining through careful design the other listed error sources, we will then be able to effectively characterize the scattering phenomenology that determines the electromagnetic penetration.

D. Thermally Stable Mechanical Baseline

The layout for GLISTIN included a pair of antennas that had a baseline spacing of 25 cm and were tilted an additional $14°$ toward nadir from the $45°$ tilt provided by the UAVSAR pod (see Fig. 4). To meet the 50-μm stability requirement from $+70\ °C$ to $-70\ °C$, a coefficient of thermal expansion (CTE) less than 1.4 ppm/°C was needed (where $CTE = \delta/B^*\Delta T$,

TABLE IV
ESTIMATED HEIGHT ACCURACY MID-SWATH (31° INCIDENCE) AFTER INSTRUMENT CALIBRATION AT 7-km ALTITUDE

Parameter	Error	Elevation Error Contribution (3 m post)	Elevation Error Contribution (30 m post)	Elevation Error Contribution (100 m post)
Phase (rad)	0.1/0.003	2.194	0.224	0.067
Baseline Length (m)	0.000033	-0.138	-0.138	-0.138
Baseline Orientation (rad)	0.0000484	0.202	0.202	0.202
Range (m)	0.083	0.071	0.071	0.071
Platform Altitude (m)	0.05	0.050	0.050	0.050
RMS Total (m)		2.209	0.343	0.268

δ is the dimensional change due to temperature, and ΔT is the change in temperature). The L-Band UAVSAR antenna panel utilized 6061-T6 aluminum face sheets with an aluminum honeycomb core. This would have provided a CTE of 22.9 ppm/°C if implemented for GLISTIN. Even a high-performance metal alloy like Invar 36 would only have a CTE of 1.98 ppm/°C over that temperature range. This drove the design of the GLISTIN antenna panel to utilize composite face sheets. Carbon fibers with a cyanate ester resin were chosen because they provide excellent thermal stability, perform well in the -70 °C regime, and are commercially available. The fibers were arranged in a quasi-isotropic layout ($[0/\pm 45/90/\underline{\text{CORE}}]_S$) using a 5-mil-thick M55J/RS-3C unidirectional tape for the face sheet layers and an aluminum 5052 aluminum honeycomb core. This panel design provided an analytical CTE of 0.05 ppm/°C which equated to less than 2 μm of dimensional change in the baseline between the two antennas.

An adverse effect of utilizing a very low CTE panel was the CTE mismatch it created when mounted into the aluminum frame that is the UAVSAR pod. For GLISTIN, it was decided to use aluminum edge clips identical to the UAVSAR design for cost effectiveness and to ensure that the bolted joint between the pod and the panel would not slip and lose alignment during temperature excursions. This meant that a long aluminum part needed to be bonded to a near-zero CTE composite panel. The stresses resulting from that configuration would have exceeded the strength of any known aerospace adhesive. To help buffer the CTE mismatch between the aluminum and the composite panel, a single layer of E-Glass ($CTE \approx 6.1$ ppm/°C) was added to the periphery of the panel (Fig. 4). The addition of the E-Glass layer to the bonded joint enabled the use of Hysol's EA9360 for the bonded joint.

The two other key mechanical contributors to the error sources were the flatness of the panel and the parallelism of the antennas. Typical manufacturing tolerances were acceptable for the flatness ($\sim$0.25 mm). To ensure that the two antennas were parallel to within 0.1° (1/10th beamwidth requirement), shims were used between the antennas and their mounting brackets. After the antennas were installed onto the panel, their parallelism was measured using a coordinate-measuring machine. No shim adjustment was needed since the antennas were aligned within tolerance.

E. Postcalibration Predicted Accuracy

If we revisit (1) and now include realistic postcalibration systematic error sources, the height error δh and the elevation measurement accuracy σ_h can be expressed as in (9) and (9a), respectively, shown at the bottom of the page.

Table IV shows the relative contribution assessed for each of the error terms at 3-, 30-, and 100-m elevation posts assuming a platform altitude of 7 km above the ground surface. The phase error evaluated at mid-swath is based on (2), where $N \approx 12$, 1100, and 12 000 looks, respectively, and we assumed a correlation of $\gamma = 0.9$. Note that $\gamma = 0.9$ was chosen as the worst case value in the near range and is generally less than what is observed in data collected over the ice. If a less conservative correlation estimate is employed when computing the phase error component to the precision, i.e., a value of 0.99 consistent with the predictions based on expected SNR, then the values in Table IV more closely match the observed precision estimates based on the observed interferometric correlation with a value of around 0.60 m for the 3-m posting. Further improvements in precision occur by effective low-pass filtering in the processing and range spectral filtering that are reflected in the data examples of Section V.

The postcalibration systematic errors are assessed as follows: The baseline length error after calibration is assumed to be 1/3

$$\delta h = \frac{\partial h}{\partial \phi}\delta\phi + \frac{\partial h}{\partial B}\delta B + \frac{\partial h}{\partial \alpha}\delta\alpha + \frac{\partial h}{\partial R}\delta R + \frac{\partial h}{\partial h_p}\delta h_p$$

$$= -\frac{R\sin(\theta)}{kB\cos(\theta-\alpha)}\delta\phi - \frac{R}{B}\tan(\theta-\alpha)\sin\theta\,\delta B + R\sin(\theta)\delta\alpha - \cos(\theta)\delta R + \delta h_p \tag{9}$$

$$\sigma_h = \sqrt{\left(\frac{\partial h}{\partial \phi}\right)^2 \sigma_\phi^2 + \left(\frac{\partial h}{\partial B}\right)^2 \sigma_B^2 + \left(\frac{\partial h}{\partial \alpha}\right)^2 \sigma_\alpha^2 + \left(\frac{\partial h}{\partial R}\right)^2 \sigma_R^2 + \left(\frac{\partial h}{\partial h_p}\right)^2 \sigma_{h_p}^2} \tag{9a}$$
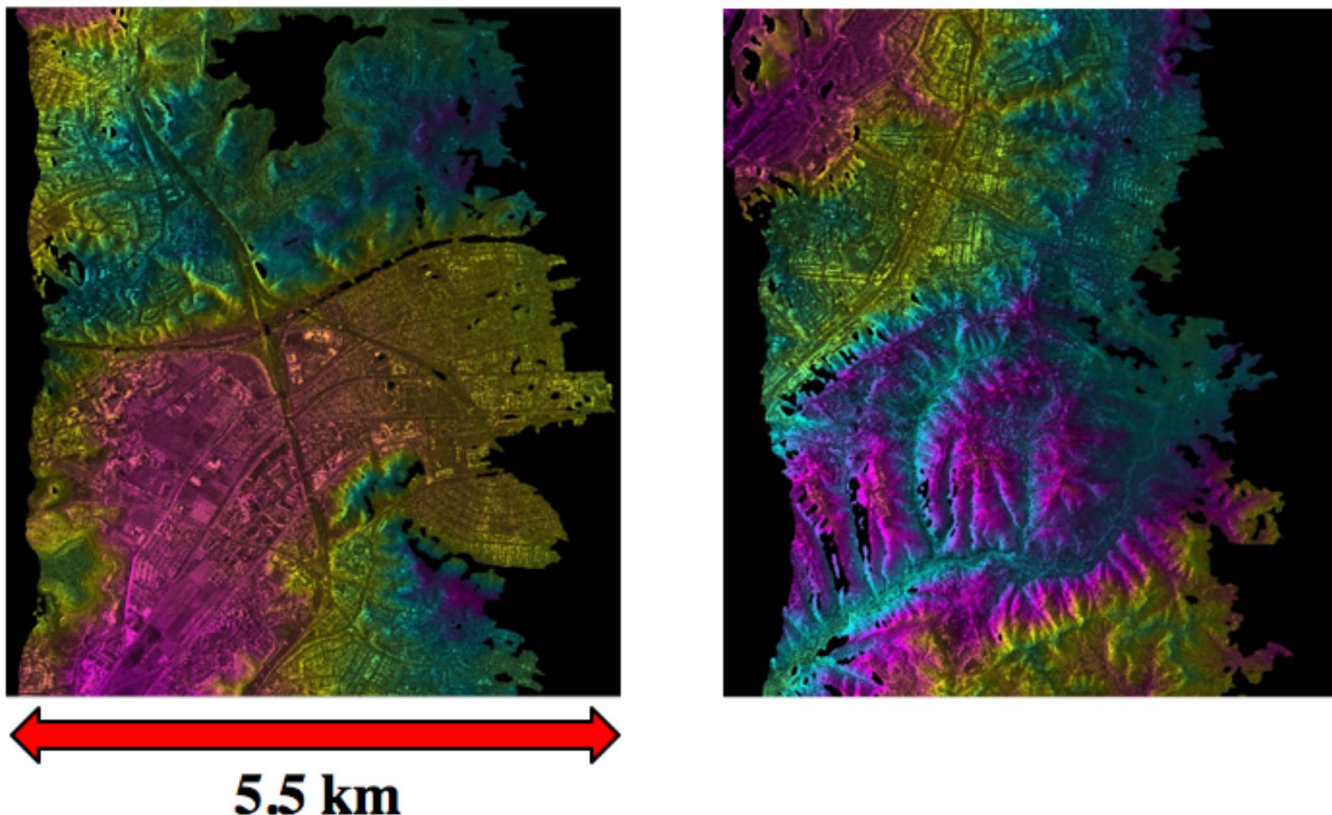
Fig. 5.   Images generated from data collected on the second Ka-band engineering test flight on March 16, 2009. The aircraft flew on a heading of 180° and imaged from San Dimas, CA, down to Irvine at an altitude of 6000 m. The swath width is about 5.5 km, and the data were processed to a height map with posting of 3 m. The height precision (as derived from the interferometric correlation) varies from about 30 cm in the near range to 3 m in the far range.
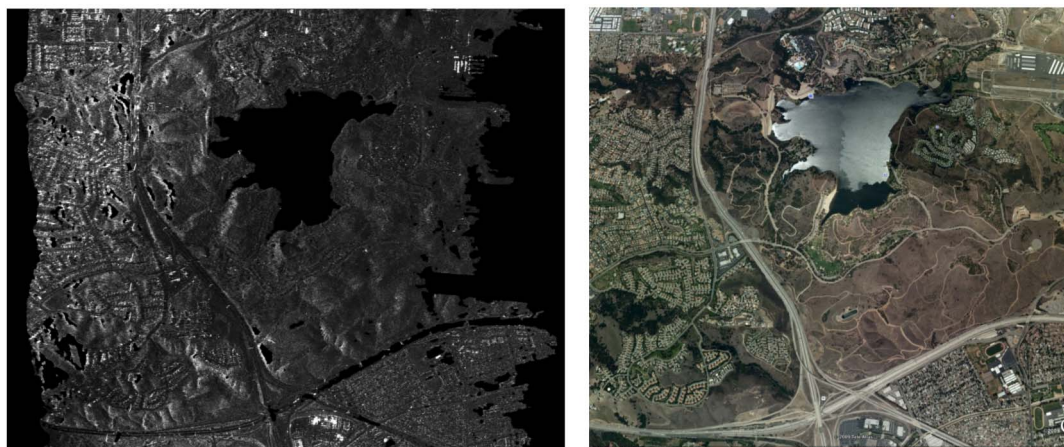

Fig. 6.   (Left) Ka-band radar backscatter image of Puddingstone Lake in San Dimas, CA, compared to (right) a corresponding image from Google Earth of the same area. The image is approximately 5.5 km by 5.5 km.

of the *a priori* surveyed value (0.1 mm) based on previous system calibrations, the baseline orientation is assumed to be limited by INU measurement accuracy (10 arcseconds), the range error is set to 1/20 of a range pixel (1.66 m) which can be measured using corner reflector data, and the platform position error is based on the DGPS accuracy of 5 cm. It must be noted that the character of the phase noise term differs from the other components in the error budget in that it is a high-frequency error term that represents point-to-point relative elevation error, whereas the other terms are effectively low-frequency terms that roughly behave as either an elevation bias or tilt across the swath. By taking orthogonal mapping swaths or via fiducial points (e.g., corner reflectors), it is possible to reduce these low-frequency errors, whereas the phase noise term reduces only as the square root of the number of additional looks. For the 3-m posting, the rms accuracy

is dominated by the phase error term that limits instrument precision (since this error is not reduced using fiducial data), whereas for the 100-m posting, there is approximate parity between the various error sources. Reflecting this back to our initial requirements in Table I, it is apparent that, to meet the glacier/coastal mapping accuracy (0.5 m at 30-m posting), the predicted postcalibration performance is sufficient with margin. However, this is not the case for the more accurate requirement for the ice sheets (10 cm at 100-m posting). In this scenario, the residual systematic errors dominate the error budget, and additional data calibration steps will be necessary to remove these biases.

IV. PROCESSING AND CALIBRATION

Processing of the Ka-band data uses a slightly modified form of the interferometric processor developed for the GeoSAR X-band/P-band dual-frequency interferometer [18]. The patch-based (a patch is a group of presummed pulses with multiple synthetic aperture lengths in duration for which the Doppler centroid is assumed constant) processor ingests raw radar data from the two interferometric channels and outputs elevation data, orthorectified image and interferometric correlation data, and a height error map giving the point-to-point statistical height accuracy based on the correlation data. The basic steps in the interferometric processing are outlined hereinafter. First, onboard motion data from the DGPS and INU are blended and placed into files with other time-varying parameter data. Processing then consists of range compression and presumming whereby the data are resampled to uniform along-track sampling along the reference track. Subsequent to presumming is first-stage motion compensation whereby the data are resampled to the best fit line parallel to the reference of the antenna position data. A range/Doppler algorithm is used for azimuth compression followed by a second stage of motion compensation whereby the data are resampled to a global reference path. Interferogram formation, spatial averaging, phase filtering, and phase unwrapping are then followed by height reconstruction where the phase data coupled with range, platform position, baseline, and Doppler data are used to reconstruct the 3-D location of each spatially averaged resolution element. The 3-D reconstructed data are then interpolated onto a uniform ground-projected grid along with the image, correlation, and height data.

Determining height from interferometric phase measurements requires knowledge of the platform position, range, baseline length and orientation, interferometric phase, wavelength, velocity, and Doppler. Estimating systematic corrections to these parameters to obtain consistently accurate topographic maps is the essence of InSAR calibration. Calibration begins with data collection over our calibration site at the Rosamond Lake bed where an array of corner reflectors is deployed in the cross-track direction. Several flight altitudes were flown to verify the stability of the calibration parameters. The data are first processed to form slant-range images. Corner reflector locations, range and along-track coordinates, in the slant-plane imagery can be predicted from the surveyed locations of the corner reflectors and platform ephemeris data. The predicted
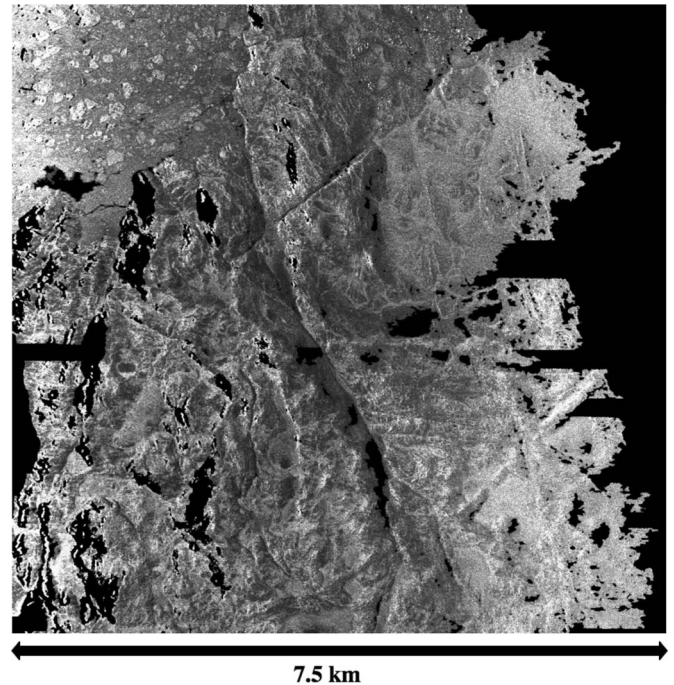

Fig. 7. Ka-band radar backscatter image with a 3-m posting that was collected on May 1, 2009, near the Greenland coast. The black regions are due to lack of correlation (less than 0.4).

range is compared with the measured range, and the difference forms the common range delay correction. Range pixel location can be determined to better than a tenth of a pixel by over-sampling the slant-plane imagery. Because range measurements to the two interferometric channels may differ, a differential range correction is computed, by measuring range offsets between the two channels. Differential range measurements are accurate to better than a hundredth of a range pixel and insure proper range registration of the channels during interferogram formation.

After determining the common and differential range corrections, the data are reprocessed, and strip map digital elevation models (DEMs) and orthorectified imagery are generated. Planimetric positions of the corner reflectors are measured using oversampled orthorectified imagery. The height of the corner reflectors is obtained by interpolating the interferometric DEM to get the height at the measured planimetric location of the corner reflector. By comparing the surveyed 3-D locations of the corner reflector array to the interferometrically observed positions, correction estimates for baseline length, baseline orientation angle, and phase are made via a least square technique. Finally, the high-accuracy DEM is used to generate a phase screen that provides elevation angle-dependent phase corrections for effects such as multipath and switch leakage (which are minimal for this system based on initial assessment of the phase screen). Radiometric calibration of the imagery using corner reflector brightness is done at this stage, completing the calibration process.

In addition to the corner reflectors at the Rosamond Lake Bed in California, we also deployed three corner reflectors at sites in Greenland which are used for *in situ* calibration to remove residual tilts or height biases. Removal of height biases
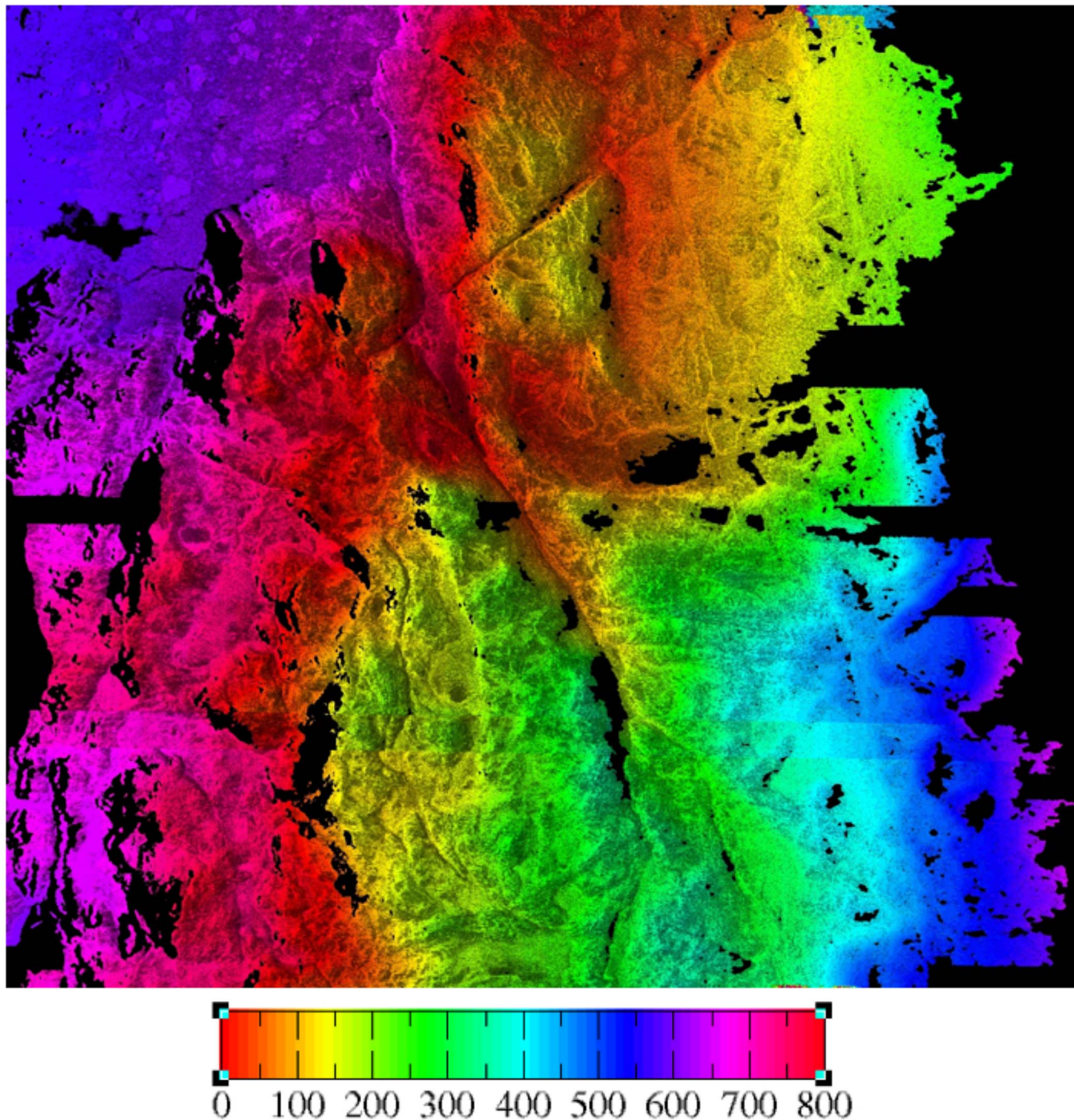
Fig. 8. Ka-band radar elevation map generated from data collected on May 1, 2009, near the Greenland coast. Elevation contours are color coded with a wrap of 800 m, i.e., from red to red represents an elevation change of 800 m.

at the centimeter level is essential for the quantitative differential penetration differences between lidar and the Ka-band radar.

V. INITIAL RESULTS AND PERFORMANCE

A. *Engineering Checkout*

The Ka-band topographic mapping instrument was developed on a tight schedule with the ultimate goal of being ready for deployment to Greenland in the spring of 2009. This necessitated a brief engineering checkout phase consisting of only three flights prior to deployment. The first flight overflew the Rosamond Lake Bed where specially constructed corner reflectors were installed and surveyed. These reflectors (1 m in the long dimension) are considerably smaller than the UAVSAR corner reflectors to avoid saturating the receiver. Additional flight lines on the second engineering were flown over a variety of terrain types to assess the Ka-band backscatter
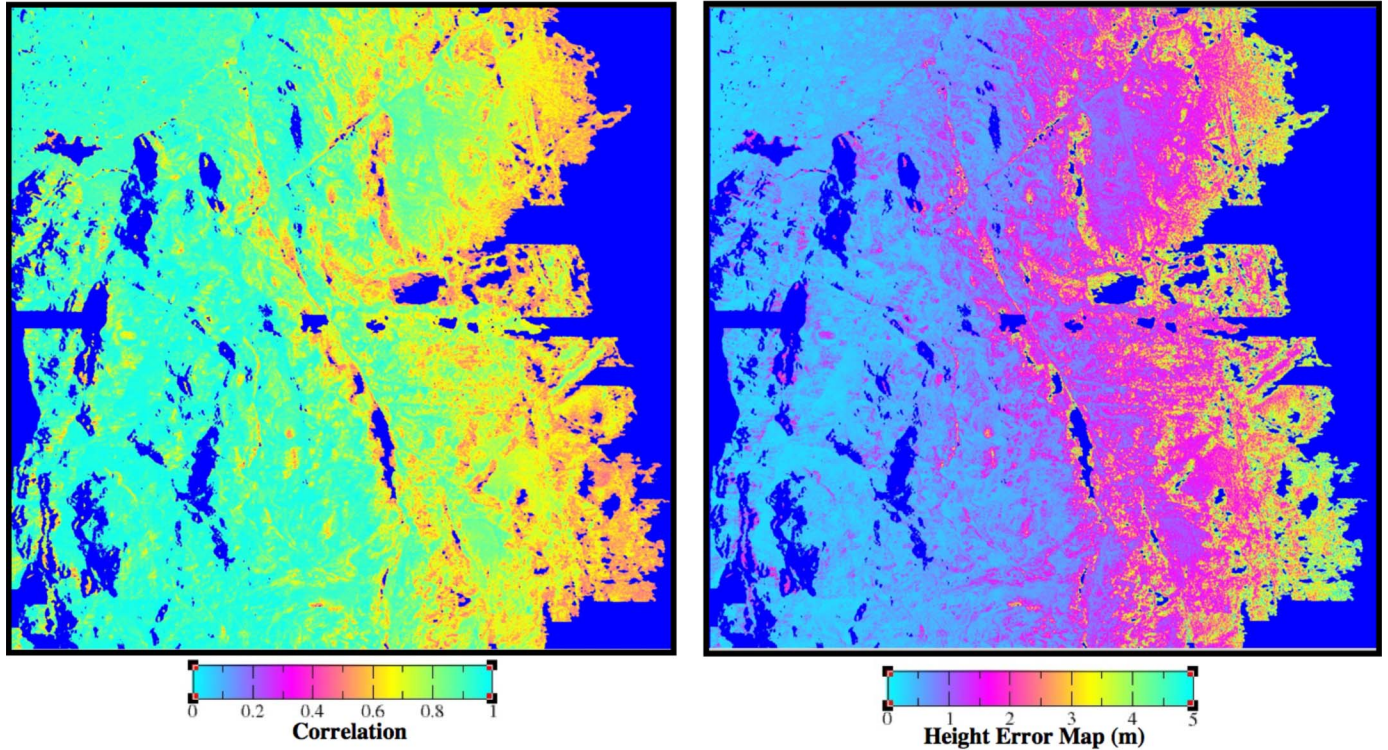
Fig. 9. (Left) Interferometric correlation and (right) height error map generated from the correlation data. Note that the relative height error varies from 30 cm in the near range to about 3 m in the far range. This relative error reduces with the scale of spatial averaging (i.e., this translates to 3-cm near-range and 30-cm far-range random error if averaged to a 30 m × 30 m posting).

characteristics and interferometric height reconstruction accuracy.

Elevation data from the first flight showed that the system was working well except for a switch leakage problem that was identified and fixed prior to the next flight. Fig. 5 shows imagery that was generated from the data collected on the second Ka-band engineering test flight on March 16, 2009. The aircraft flew on a heading of 180° and imaged from San Dimas, CA, down to Irvine at an altitude of 6000 m. The swath width is about 5.5 km, and the data were processed to a height map with posting of 3 m. The height precision varies from about 30 cm in the near range to 3 m in the far range. Fig. 6 shows a Ka-band radar backscatter image (left) of Pudding-stone Lake in San Dimas, CA, compared to a corresponding image from Google Earth (right) of the same area. The imaged area is approximately 5.5 km by 5.5 km. Despite the reduced image contrast compared to longer wavelength SARs (e.g., X- or L-band), the urban area, roads, and lake are all clearly visible.

B. Initial Results Over Ice

The Ka-band system was deployed to Greenland from May 1 to 13, 2009, and mapped more than 35 000 km² (9 h of data collection time) over coastal glaciers and at higher elevation over dry firn, including Greenland's Summit. Fig. 7 shows a Ka-band backscatter image taken over a relatively rugged area along the West coast of Greenland at 69.1° N latitude and 49.7° W longitude (just South of Jakobshavn glacier) from an altitude of 8 km. Backscatter from the surface is relatively

bright, except for a few dark regions, where interferometric correlation is correspondingly low. Low correlation prevented successful phase unwrapping, resulting in some pixels not being mapped (indicated by black pixels). Fig. 8 shows the corresponding height map with the image brightness indicating radar backscatter and elevation shown by color contours with a height wrap of 800 m (i.e., red to red corresponds to an 800-m elevation change). One of the unique features of radar interferometric mapping systems is the ability to generate statistical height error maps σ_h for each pixel using the interferometric correlation via the relation

$$\sigma_h = \frac{\partial h}{\partial \phi} \sigma_\phi$$

$$= \frac{1}{2\pi k_z} \sigma_\phi$$

$$= \frac{1}{\sqrt{2N_L}} \frac{\lambda R \sin(\theta)}{2\pi B \cos(\theta - \alpha)} \sqrt{\frac{1 - \gamma^2}{\gamma^2}}. \qquad (10)$$

Fig. 9 shows the corresponding correlation and height error data. The decreased correlation and resulting increasing height errors from near to far ranges are due to a reduction in signal-to-noise ratio from the increased range and antenna pattern effects. Height errors vary from 30 cm in the near range to about 3 m in the far range for 3 m × 3 m pixels. When compared with our initial design and performance predictions in Table III, the performance in the near range actually exceeds our expectations. This can be attributed to presumming and processing gains that were not accounted for in the system

Fig. 10. Graphic (courtesy of John Sonntag, NASA) showing data collection and calibration sites. The gray-shaded lines show regions of GLISTIN data collection. The overlapping black lines show the tracks collected by the ATM. Calibration sites were established at NSF's Summit Camp and CIRES' Swiss Camp and JAR1 sites.

engineering predictions and result in a performance margin that enables a swath that can extend up to 7.5 km.

Spatial averaging of the data from 3 to 100 m results in a 30-fold increase in height precision, and thus, this component of the error budget falls below the 10-cm error requirement for 100-m pixels. However, as indicated in Table IV, at 100-m posting, the systematic errors will dominate the error budget and further correction so that this requirement that can be met will require more sophisticated processing and correction (through crossing lines and/or correction with auxiliary data). In the glacier/coastal regions, the tenfold reduction in random errors, combined with the systematic errors predicted in Table IV (residual errors after routine correction and cali-

bration), will meet the mapping requirement of 0.5-m height accuracy at 30-m posting.

VI. GREENLAND EXPERIMENT

In this paper, we have presented just one sample data scene from Greenland to exhibit the initial performance over the ice. However, Fig. 10 shows an overview of the extent of Greenland data collection locations, including calibration sites. The gray-shaded regions indicate the locations of GLISTIN mapping, all of which occurred with the G-III staging out of Thule Air Force base. All planned data were collected for a total of six flights. For the first flight day out of Thule (May 4, 2009), we flew

over NSF's Summit Station where three corner reflectors were deployed and precision surveyed near Summit Station. It is at these high elevations with dry firn cover that we expect penetration to be the greatest. Then, GLISTIN collected data in a transect to CIRES' Swiss Camp, continuing to the coast. Three corner reflectors were also deployed and precision surveyed at the Swiss Camp and JAR1 locations of the Greenland Climate Network [19].

The GLISTIN transect height data are to be compared (in a future publication) with the NASA Wallops ATM lidar on the P3. Referring again to Fig. 10, the ATM flight path is indicated by black solid lines (the P3 was staging out of Sondestrom/Kangerlussuaq during this time). All GLISTIN/ ATM comparative data were collected within 24 h of each other, and at lower elevations (less than 2000), the overflights occurred within a few hours.

On May 5, 2009, GLISTIN mapped a large portion of Jakobshavn glacier with a series of overlapping racetracks. A flight on May 6, 2009, completed the mapping.

The second set of data collections (three flights) was moved earlier than anticipated due to the C17 air transport of the L-band UAVSAR pod being delayed. For this reason, we did not get to observe any changes due to melting (which was one of our original objectives). However, due to the highly dynamic nature of the region, we decided to continue with the planned revisit to Jakobshavn. The final two flights on May 12 and May 13, 2009, repeated the Jakobshavn mapping. Initial "quick-look" observations in the field indicated mapping features moving by 1 km in a six-day interval.

On May 11, 2009, we flew over the Watson River glacial outlet (just south of Kangerlussuaq—see Fig. 10), transitioning up onto the ice sheet where the supraglacial lakes form. *In situ* observations included topographic transects and characterization of surface roughness and vegetation (in nonsnow-covered regions).

VII. Conclusion and Future Work

In this paper, we have detailed the implementation and the initial performance of the first Ka-band single-pass InSAR. This proof-of-concept demonstration was achieved by adapting the L-band UAVSAR system for operation at the higher frequency and housing two cross-track antennas with a stable baseline within the UAVSAR pod. Successful engineering flights demonstrated height mapping capability over urban areas with high precision. These were followed by a comprehensive campaign to Greenland, including two calibration sites, ground activities, and collaborative flights with the ATM sensor. As shown in this paper, the initial performance results for the Ka-band GLISTIN instrument over rugged ice and topography exceed engineering predictions and meet the requirements for height precision. Systematic and penetration biases have yet to be assessed with precision calibration.

As part of our continuing effort, all the data collected in Greenland will be processed into DEM strip maps. Surveyed corner reflectors, GPS stations, other known reference points (e.g., the IceSAT calibration site at Summit), and ATM data will be used to derive penetration offsets. The penetration data

will be compiled, quantified, and characterized as a function of incidence angle and snow characteristics. These data will be used to derive empirical or model-based predictions of penetration depth.

The penetration-corrected strip map data will be mosaicked to form surface-topography DEM maps. Further analysis of these products will focus on science phenomenology that can be observed in these products in conjunction with collaborative sensors and ground observations.

References

[1] A. Shepherd and D. Wingham, "Recent sea-level contributions of the Antarctic and Greenland Ice Sheets," *Science*, vol. 315, no. 5818, pp. 1529–1532, Mar. 2009.

[2] R. Thomas, C. Davis, E. Frederick, W. Krabill, Y. Li, S. Manizade, and C. Martin, "A comparison of Greenland ice-sheet volume changes derived from altimetry measurements," *J. Glaciol.*, vol. 54, no. 185, pp. 203–210, Mar. 2008.

[3] H. D. Pritchard, R. J. Arthern, D. G. Vaughn, and L. A. Edwards, "Extensive dynamic thinning on the margins of the Greenland and Antarctic ice sheets," *Nature*, vol. 461, no. 7266, pp. 971–975, Oct. 2009.

[4] D. Moller, B. Heavey, R. Hodges, S. Rengarajan, E. Rignot, F. Rogez, G. Sadowy, M. Simard, and M. Zawadzki, "The Glacier and Land Ice Surface Topography Interferometer (GLISTIN): A novel Ka-band digitally beamformed interferometer," in *Proc. ESTC Conf.*, University Park, MD, 2006.

[5] P. A. Rosen, S. Hensley, K. Wheeler, G. Sadowy, T. Miller, S. Shaffer, R. Muellerschoen, C. Jones, H. Zebker, and S. Madsen, "UAVSAR: A new NASA airborne SAR system for science and technology research," in *Proc. IEEE Conf. Radar*, Apr. 24–27, 2006, pp. 22–29.

[6] W. Krabill, R. Thomas, C. Martin, R. Swift, and E. Frederick, "Accuracy of airborne laser altimetry over the Greenland ice sheet," *Int. J. Remote Sens.*, vol. 16, no. 7, pp. 1211–1222, May 1995.

[7] D. Moller, B. Heavey, E. Rignot, G. Sadowy, M. Simard, and M. Zawadzki, "A novel Ka-band digitally beamformed interferometric synthetic aperture radar for glacier and ice-sheet topographic mapping: Concept and technology development," in *Proc. EUSAR*, Friedrichshafen, Germany, 2008.

[8] S. R. Rengarajan, M. S. Zawadzki, and R. E. Hodges, "Design, analysis and development of a large Ka-band array for digital beam-forming

application," *IEEE Trans. Antennas Propag.*, vol. 57, no. 10, pp. 3103–3109, Oct. 2009.

[9] E. Rodriguez and J. Martin, "Theory and design of interferometric synthetic aperture radars," in *Proc. Inst. Elect. Eng.—E*, Apr. 1992, vol. 139, no. 2, pp. 147–159.

[10] P. A. Rosen, S. Hensley, F. Li, I. Joughin, S. Madsen, and D. Goldstein, "Synthetic aperture radar interferometry," *Proc. IEEE*, vol. 88, no. 3, pp. 333–382, Mar. 2000.

[11] F. T. Ulaby, R. Moore, and A. K. Fung, *Microwave Remote Sensing, Active and Passive*. Norwood, MA: Artech House, 1986.

[12] R. Forsberg, K. Keller, and S. M. Jacobsen, "Airborne lidar measurements for cryosat validation," in *Proc. IGARSS*, 2002, vol. 3, pp. 1756–1758.

[13] A. K. Fung and H. J. Eom, "Application of a combined rough surface and volume scattering theory to sea ice and snow backscatter," *IEEE Trans. Geosci. Remote Sens.*, vol. GE-20, no. 4, pp. 4528–4536, Oct. 1982.

[14] P. Vincent, N. Steunou, E. Caubet, L. Phalippou, L. Rey, E. Thouvenot, and J. Verron, "AltiKa: A Ka-band altimetry payload and system for operational altimetry during the GMES period," *Sensors*, vol. 6, no. 3, pp. 208–234, Mar. 2006.

[15] V. I. Lytle and K. C. Jezek, "Dielectric permittivity and scattering measurements of Greenland firn at 26.5–40 GHz," *IEEE Trans. Geosci. Remote Sens.*, vol. 32, no. 2, pp. 290–295, Mar. 1994.

[16] G. A. Sadowy, A. C. Berkun, W. Chun, E. Im, and S. L. Durden, "Development of an advanced airborne precipitation radar," *Microw. J.*, vol. 46, no. 1, pp. 84–98, Jan. 2003.

[17] F. T. Ulaby and M. C. Dobson, *Handbook of Radar Scatttering Statistics for Terrain*. Norwood, MA: Artech House, 1989.

[18] S. Hensley, T. Michel, S. Madsen, E. Chapin, and E. Rodriguez. (2004, Jul.). Software for generating strip maps from SAR data. [Online]. Available: http://www.techbriefs.com/content/view/1727

[19] K. Steffen, J. E. Box, and W. Abdalati, "Greenland climate network: GC-Net," in *CRREL 96-27 Special Report on Glaciers, Ice Sheets and Volcanoes*, S. C. Colbeck, Ed. Hanover, NH: USACE Cold Regions Res. Eng. Lab., 1996, pp. 98–103.

Scott Hensley received the B.S. degree in mathematics and physics from the University of California, Irvine, and the Ph.D. degree in mathematics from the State University of New York at Stony Brook, where he specialized in the study of differential geometry.

Subsequent to graduating, he was with the Hughes Aircraft Company, working on a variety of radar systems, including the Magellan radar. In 1992, he joined the Staff of the Jet Propulsion Laboratory, California Institute of Technology, Pasadena, where he is currently studying advanced radar techniques for geophysical applications. His research has involved using both stereo and interferometric data acquired by the Magellan spacecraft at Venus. He has worked with ERS-1, JERS-1, and SIR-C data for differential interferometry studies of earthquakes and volcanoes. His current research also includes studying the amount of penetration into the vegetation canopy using simultaneous L- and C-band TOPSAR measurements and repeat-pass airborne interferometry data collected at lower frequencies (P-band). He was the Chief Scientist of GeoSAR, a simultaneous X- and P-band radar interferometer for mapping above and beneath the canopy that is now commercially operated by Earthdata International. He was the Technical Lead of the Interferometric Processor Development Team of the Shuttle Radar Topography Mission, a shuttle-based interferometric radar used to map the Earth's topography between $\pm 60°$ latitude. He is currently the Principal Investigator of the UAVSAR NASA program that is developing a repeat-pass radar interferometry capability for use on conventional or unmanned aerial vehicles. Recently, he began working with the Goldstone Solar System Radar to generate topographic maps of the lunar surface.

Gregory A. Sadowy received the B.S.E.E. degree in electrical engineering from the Rensselaer Polytechnic Institute, Troy, NY, and the Ph.D. degree in electrical engineering from the University of Massachusetts (UMass), Amherst, where he specialized in radar remote sensing.

While at UMass, he was a member of the Microwave Remote Sensing Laboratory and a NASA Graduate Research Fellow. In collaboration with NASA's Jet Propulsion Laboratory (JPL), California Institute of Technology, Pasadena, he developed a 95-GHz Airborne Cloud Profiling Radar. In 1999, he joined the Radar Science and Engineering Section, JPL. He has been responsible for the development of the Second-Generation Airborne Precipitation Radar RF electronics and the UAVSAR active electronically scanned antenna and has participated in the development of other airborne radar systems, including the UAVSAR Ka-band interferometer. He is currently the Supervisor of the Radar Technology Group, JPL, and develops RF, analog, and digital technology for advanced spaceborne and airborne radar systems. His areas of particular interest are active electronically scanned arrays and millimeter-wave radar systems.

Delwyn Moller received the B.E. (Hons) and M.E. (with distinction) degrees from the University of Auckland, Auckland, New Zealand, and the Ph.D. degree in electrical engineering from the University of Massachusetts, Amherst.

She is currently a Senior Engineer with Remote Sensing Solutions (RSS), Inc., Barnstable, MA. Since joining RSS, she has continued her development of novel remote sensing systems. She is the Principal Investigator (PI) for a NASA International Polar Year program that developed and demonstrated Ka-band synthetic aperture radar interferometry for mapping ice surface topography. She is also the PI of the development of an airborne Ka-band multibaseline radar interferometer to support the Surface Water Ocean Topography satellite mission and for focused science observations of terrestrial fresh water hydrology and physical oceanography processes. Prior to joining RSS, she was a Radar System Engineer with the NASA Jet Propulsion Laboratory, where she was the PI and a Coinvestigator on many research projects, including radar remote sensing of the ocean, soil moisture, cryosphere, and surface-water bodies.

Dr. Moller was a corecipient of the NASA Space Act award for "A Ka-Band Imaging Radar for Hazard Detection and Avoidance of Planetary Landers" and has received two NASA Technology Brief awards.

Charles D. Fisher was born in Michigan. He received the B.S. degree in aeronautical and astronautical engineering from Purdue University, West Lafayette, IN, in 2003.

He is currently a Mechanical Engineer with the Jet Propulsion Laboratory, California Institute of Technology, Pasadena, where he has designed, integrated, and tested a deployable boom for the Aquarius instrument; helped build the L-Band UAVSAR instrument; repaired the Tunable Laser Spectrometer instrument; and designed and tested a 2-DOF fiber optic positioner for the Wide-Field Multi-Object Spectrometer instrument. He previously worked for the Naval Air Systems Command (NAVAIR), Patuxent River, MD, where he was the Lead Structural Engineer for the EA-6B "Prowler" aircraft and provided engineering support for the A/V-8B "Harrier" and EA-18G "Growler" aircraft. He was the Lead Author on the paper "Cobra: A Two Degree of Freedom Fiber Optic Positioning Mechanism" published at the 2009 IEEE Aerospace Conference and coauthored the paper "The Telescopic Wing: An Aerodynamic Perspective" published at the 2003 AIAA Region III Student Conference.

Thierry Michel received the Ph.D. degree in physics from the University of California, Irvine, in 1990.

From 1991 to 1993, he was a Postdoctoral Fellow with the Georgia Institute of Technology, Atlanta. Then, he became a Postdoctoral Fellow and a Member of Technical Staff with the Jet Propulsion Laboratory, California Institute of Technology, Pasadena, where he is currently working on SAR processing algorithms and on the estimation of geophysical parameters from SAR data.

Mark Zawadzki (S'95–M'97) was born in Sarnia, ON, Canada, in 1965. He received the B.E.Sc. degree from the University of Western Ontario, London, ON, in 1988 and the M.S. degree in electrical engineering from the University of Massachusetts, Amherst, in 1997.

Currently, he is a Senior Engineer with the Jet Propulsion Laboratory, California Institute of Technology, Pasadena, working in the Spacecraft Antenna Research Group. His research interests include microstrip patch arrays, microstrip reflectarrays, and waveguide slot arrays.

Eric Rignot received the B.Eng. degree from the Ecole Centrale des Arts et Manufactures, Paris, France, and the M.S.A.E. and M.S.E.E. degrees and in 1991 the Ph.D. degree from the University of Southern California (USC), Los Angeles.

From 1986 to 1988, he was a Research Assistant with the Department of Aerospace Engineering, USC, working on fluid dynamics imaging techniques. In 1988, he joined the Jet Propulsion Laboratory (JPL), California Institute of Technology, Pasadena, as a Member of Technical Staff, working on sea ice remote sensing, forestry studies, radar polarimetry, and radar interferometry. In 1993, his research interests concentrated on glaciology applications of SAR remote sensing. In 2007, he joined the Department of Earth System Science, University of California, Irvine, as a full Professor, while remaining a Joint Faculty Appointee by the Office of the Chief Scientist at JPL. His research interests include the mass balance of ice sheets, ice motion mapping in Antarctica, ice sheet modeling, and ice–ocean interactions using field data, remote sensing data, and numerical models.